

Chemical Science

Accepted Manuscript

This article can be cited before page numbers have been issued, to do this please use: Z. Pang, Q. Li, Y. Jia, W. Yan, J. Qi, Y. Guo, F. Hu, D. Zhou and X. Jiang, *Chem. Sci.*, 2021, DOI: 10.1039/D1SC03056F.



This is an Accepted Manuscript, which has been through the Royal Society of Chemistry peer review process and has been accepted for publication.

Accepted Manuscripts are published online shortly after acceptance, before technical editing, formatting and proof reading. Using this free service, authors can make their results available to the community, in citable form, before we publish the edited article. We will replace this Accepted Manuscript with the edited and formatted Advance Article as soon as it is available.

You can find more information about Accepted Manuscripts in the [Information for Authors](#).

Please note that technical editing may introduce minor changes to the text and/or graphics, which may alter content. The journal's standard [Terms & Conditions](#) and the [Ethical guidelines](#) still apply. In no event shall the Royal Society of Chemistry be held responsible for any errors or omissions in this Accepted Manuscript or any consequences arising from the use of any information it contains.

ARTICLE

Controlling pyridinium-zwitterionic ligand ratio on atomically precise gold nanoclusters allowing for eradicating Gram-positive drug-resistant bacteria and retaining biocompatibilityReceived 00th January 20xx,
Accepted 00th January 20xx

DOI: 10.1039/x0xx00000x

Zeyang Pang^{a,b}, Qizhen Li^a, Yuexiao Jia^a, Weixiao Yan^a, Jie Qi^a, Yuan Guo^c, Fupin Hu^d, Dejian Zhou^{*,b}, and Xingyu Jiang^{*,a}

Abstract: Infections caused by multidrug-resistant (MDR) bacteria are an increasing global healthcare concern. In this study, we developed a dual-ligand-functionalised Au₂₅(SR₁)_x(SR₂)_{18-x}-type gold nanocluster and determined its antibacterial activity against MDR bacteria strains. The pyridinium ligand (SR₁) provided bactericidal potency and the zwitterionic ligand (SR₂) enhanced the stability and biocompatibility. By optimising the ligand ratio, our gold nanocluster could effectively kill MDR Gram-positive bacteria via multiple antibacterial actions, including inducing bacterial aggregation, disrupting bacterial membrane integrity and potential, and generating reactive oxygen species. Moreover, combining the optimised gold nanocluster with common antibiotics could significantly enhance the antibacterial activity against MDR bacteria both *in vitro* and animal models of skin infections. Furthermore, the fluorescence of the gold nanocluster at the second near-infrared (NIR-II) biological window allowed for the monitoring of its biodistribution and body clearance, which confirmed that the gold nanoclusters had good renal clearance and biocompatibility. This study provides a new strategy to combat the MDR challenge using multifunctional gold nanomaterials.

Keywords: antibiotics, Au₂₅(SR)₁₈ nanocluster, combinational therapy, MRSE, pyridinium ligand, zwitterionic ligand

^a Department of Biomedical Engineering, Southern University of Science and Technology, No 1088, Xueyuan Rd, Nanshan District, Shenzhen, Guangdong 518055, P. R. China

^b School of Chemistry and Astbury Centre for Structural Molecular Biology, University of Leeds, Leeds LS2 9JT, United Kingdom

^c School of Food Science and Nutrition and Astbury Centre for Structural Molecular Biology, University of Leeds, Leeds LS2 9JT, United Kingdom

^d Institute of Antibiotics, Huashan Hospital, Fudan University, Shanghai 200040, P. R. China

Electronic Supplementary Information (ESI) available: [details of any supplementary information available should be included here]. See DOI: 10.1039/x0xx00000x



Introduction

Since the discovery of antibiotics in 1928, the unrestrained global use of antibiotics has imposed a highly selective pressure on all bacterial species, which has accelerated the acquisition and accumulation of drug-resistant genes via horizontal transmission.¹ Several multidrug-resistant (MDR) pathogens, or the so-called ‘superbugs,’ have emerged over the past 50 years.^{2,3} Moreover, some drug-resistant bacteria that were previously considered less harmful, like Methicillin-resistant *Staphylococcus epidermidis* (MRSE), have gained much attention due to its role in the development of drug-resistant strains.^{4,5} The widespread of MRSE inevitably increases the risk of infection and promotes intra- and inter-species horizontal transfer of the MDR gene.⁶ MDR-related infections has imposed a significant burden on the world economy and healthcare systems, yet, the development of new antibiotics has largely stalled over the past 20 years.⁷ Therefore, there is an urgent need to develop new strategies to address this significant global health problem.

Recently, gold nanomaterials, including gold nanoparticles (GNPs),^{8,9,10} gold nanorods (GNRs)¹¹ and gold nanoclusters (GNCs),^{12,13} have emerged as potentially effective antibacterial agents. They can exhibit several antibacterial actions, such as delivering antibiotics, producing reactive oxygen species (ROS) and offering photothermal treatments.^{14,15} Among which, the sub-2 nm GNCs have a distinct advantage of readily renal clearance, which can greatly reduce the potential long term toxicity.¹⁶ Recent studies have focused on synthesising atomically precise GNCs¹⁷ to achieve better quality control, which is important for potential clinical approval. Among all formula-precise GNCs, the Au₂₅(SR)₁₈ type GNC is the most widely studied owing to its high stability, low toxicity, feasible preparation and stable near-infrared (NIR) fluorescence,¹⁸ making it a powerful tool for bioimaging, drug delivery and

therapy.^{19,20} However, most Au₂₅(SR)₁₈ GNCs reported so far are capped with a single-type ligand, limiting the ability to tune their biocompatibility and antibacterial potency, as the requirements for the two are often incompatible. Consequently, most antibacterial nanomaterials have only demonstrated effectiveness *in vitro* but not *in vivo*.¹²

Herein, we synthesised a pyridinium-zwitterionic dual-ligand functionalised Au₂₅(SR₁)_x(SR₂)_{18-x} GNC to address MDR bacteria-induced infections, especially MRSE (**Figure 1A**). The pyridinium ligand is derived from cetylpyridinium chloride (CPC), a commercial mouth mucosa aseptic additive approved by the US Food and Drug Administration, which affords antibacterial ability although it suffers poor prospect of *in vivo* applications.^{21,22} The zwitterionic (ZW) ligand was introduced due to its biocompatibility, biosafety, and low biofouling properties.^{23,24} Previously, our group and other researchers showed that ZW ligand-coated nanoparticles are highly stable, biocompatible and strongly resist biofouling.^{25,26} By adjusting the GNC surface capping pyridinium/ZW ligand ratio, GNCs that displayed low cytotoxicity and excellent antibacterial activity against clinically isolated Gram-positive drug-resistant species were obtained. Besides, we discovered that the combination of our GNCs with conventional antibiotics could significantly enhance the bactericidal potency against MRSE, allowing us to overcome MDR bacterial infections at the cellular level and *in vivo* skin infection models. Furthermore, we exploited the stable NIR-II fluorescence of our GNC to directly monitor the *in vivo* biodistribution, revealing that the GNC was efficiently cleared without inducing observable long-term toxic effects. All these results show that our optimised Au₂₅(SR₁)_x(SR₂)_{18-x} GNC is a new generation of multifunctional fluorescent nanomaterial for treating MDR bacterial infections induced by Gram-positive strains.

View Article Online
DOI: 10.1039/D1SC03056F



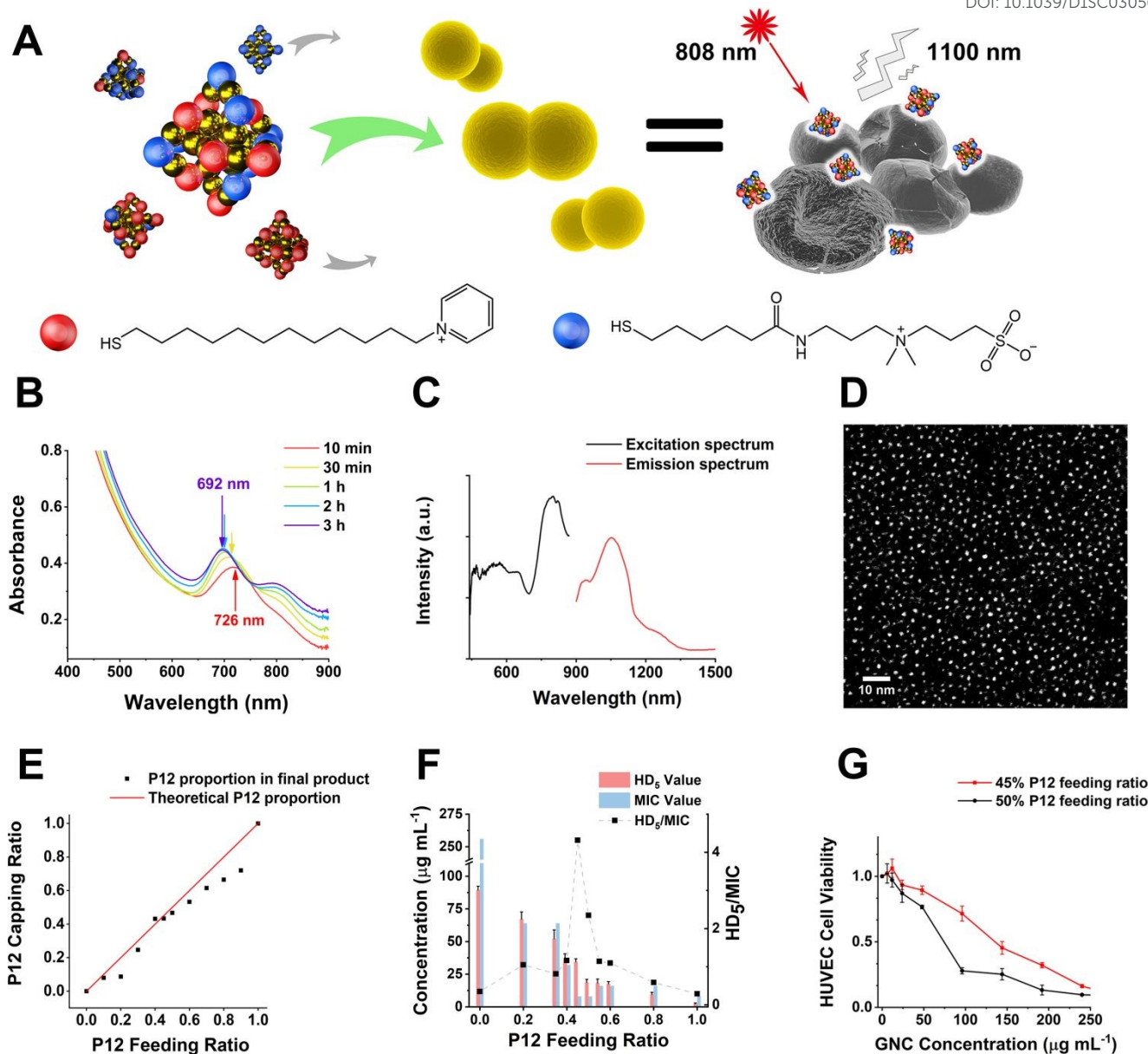


Figure 1. (A) A schematic diagram of this study. GNCs with a specific P12/C5 composition aggregate planktonic bacteria by interacting with the bacterial cell envelope while maintaining good biocompatibility. Local interactions of GNCs with bacteria cause cell content leakage and structural deformation, which induce cell death. The distribution of GNCs is tracked using NIR fluorescence upon excitation with 808 nm laser. Golden spheres indicate gold atoms, red spheres indicate the P12 ligands, blue spheres indicate the C5 ligands. (B) Time-dependent evolution of the UV-vis spectra of 100% C5-capped GNC (representative species) during the synthesis process. (C) NIR fluorescence excitation (black line, monitored with $\lambda_{EM} = 1100$ nm) and emission (red line, $\lambda_{EX} = 810$ nm) spectra of 100% C5-capped GNC. (D) Double spherical aberration-corrected TEM images (scale bar: 10 nm) of 100% C5-capped GNC prepared on an ultra-thin carbon film copper mesh. The UV-vis spectra, NIR fluorescence spectra and TEM images of GNCs with other P12/C5 composition has no obvious differences with this representative species. (E) A plot of the GNC surface P12 capping ratio versus the P12-feeding ratio. The red line indicates the theoretic output, assuming no ligand affinity difference, whereas the black dots represent the actual P12 ratio. (F) $\text{HD}_{50}/\text{MIC}$ values for dual-ligand GNCs prepared under different P12 feeding ratio. The greater the $\text{HD}_{50}/\text{MIC}$, the higher the biosafety and antibacterial ability of the material. A sudden change in haemolytic potency appears as the feeding ratio approaches 50% (MIC value is from anti-*S.aureus* result). (G) Comparison of the cytotoxicity of the 45% and 50% P12 GNCs toward human umbilical vein endothelial cells (HUVECs) with 24-h incubation.

Results and Discussion

Synthesis and characterisation of $\text{Au}_{25}(\text{SR}_1)_x(\text{SR}_2)_{18-x}$ -type GNCs

In this study, alkyl-thiolated ZW and pyridinium ligands (abbreviated as C5 and P12, hereafter) were synthesised, and their chemical structures were confirmed by NMR and mass spectrometry (MS), respectively (see **Supporting Information**

(SI), **Figure S1-9**). GNCs with different surface ligand capping were then prepared by varying the feeding ratios between 100% C5 and 100% P12 ligands. The formation of Au_{25} NC was characterised by a UV-visible spectrum (UV-vis) absorption peak at ~ 690 nm with a shoulder at ~ 810 nm.²⁷ The characteristic absorption peak was blue-shifted from ~ 730 to ~ 690 nm during the first 2 h. Then, the spectrum for Au_{25} NC stabilised after 3 h, suggesting that the synthesis of Au_{25} NC



was complete (**Figure 1B**).²⁸ Using this reaction time, we synthesised GNCs with the increasing feeding ratio of P12 (from 0% to 100%). All mixed P12/C5 groups successfully produced the $\text{Au}_{25}(\text{P12})_x(\text{C5})_{18-x}$ -type GNCs, indicated by obvious absorption peaks at 690 nm (see **SI, Figure S10**).

Under 808 nm laser excitation, the GNCs showed a strong fluorescence peak at ~1100 nm with a shoulder at ~950 nm, regardless of the ligand composition, which is consistent with the previous report²⁹ (**Figure 1C**). Such fluorescent characteristics are ideal for sensitive fluorescence imaging in the second near-infrared (NIR-II) biological window, which benefits enhanced tissue penetration depth and resolution.³⁰ Despite having a moderate absolute fluorescence quantum yield (0.54%) compared with small molecular NIR-II emitting dyes,^{31,32} our GNCs exhibited higher stability, biocompatibility and anti-photobleaching properties, which are extremely beneficial to bioimaging.³³

The GNC size prepared under different ligand feeding ratios were measured by double spherical aberration-corrected TEM (DSAC-TEM) analysis, which revealed the GNC granule size to be around 1.2 nm with negligible difference between each different-ligand group (**Figure 1D and Table 1**). These results are consistent with the ultra-small size of Au_{25} NCs reported in the literature.³⁴

In addition, the zeta potential of GNCs prepared under different P12 ligand feeding ratios were measured and summarized in **Table 1**. The zeta potential of GNCs was gradually and progressively shifted from around -5 mV to > +70 mV as the P12 ligand feeding ratio was increased from 0 to 100%, indicating successful incorporation of P12 ligand onto the GNC surface.

The GNCs were further characterised by electrospray ionisation MS (ESI-MS), which yielded the general molecular formula of diverse $\text{Au}_{25}(\text{P12})_x(\text{C5})_{18-x}$ ($x = 0-18$, depending on the P12/C5 feeding ratio, see **SI, Figure S11**). After mass deconvolution, the exact mass of the dominant peaks was matched with the theoretical molecular weight (**Table 1 and, SI, Table S1**). The relative abundance of each GNC was derived from its corresponding peak in the mass spectrum³⁵ and the relationship between the GNCs surface ligand composition and corresponding ligand feeding ratio was summarized in **Table 1**. It is apparent that except for those prepared with 100% P12 or 100% C5, all other GNCs prepared were a mixture of differently formulated $\text{Au}_{25}(\text{P12})_x(\text{C5})_{18-x}$ GNCs, which could be explained by the putative forming mechanism of GNCs. Upon adding the dual-ligand solution to chloroauric acid, the thiol groups quickly reduced the trivalent Au(III) ions to Au(I) to form the Au(I)-ligand complexes³⁶. Due to the random reduction and combination of Au(I) with different capping ligands, the complex units would have multiple types. The subsequent addition of sodium borohydride to reduce Au(I) for cluster formation and sodium hydroxide (for controlling ligand etching ability) allowed the precisely reduction of some Au(I)-ligand complex to Au(0), forming a stochastic mixture of dual-ligand capped GNCs with a variety of ligand capping ratios³⁷. However, controlled mainly by our ligand feeding ratio, this synthesis condition could allow for some specific GNCs to be the main product. The relative abundance of each GNC formulation could be derived from the corresponding MS peak intensity.³⁵

Table 1. Characterisation of $\text{Au}_{25}(\text{P12})_x(\text{C5})_{18-x}$ GNCs prepared at different P12 feeding ratios.

P12 ratio in feeding (%)	Zeta potential \pm SD (mV)	Size \pm SD (nm)	Primary product (P12/C5)	Secondary product(s) (P12/C5)	Deconvoluted MW (Da)
0	-4.7 \pm 1.1	1.18 \pm 0.21	0/18	-	11282
10	8.8 \pm 0.6	1.15 \pm 0.23	1/17	2/16	11176
20	14.1 \pm 2.0	1.21 \pm 0.32	1/17	2/16	11167
30	24.1 \pm 0.9	1.11 \pm 0.41	4/14	5/13	10954
40	36.3 \pm 2.3	1.15 \pm 0.22	7/11	8/10	10710
45	37.5 \pm 1.6	1.19 \pm 0.24	8/10	7/11 & 9/9	10708
50	43.3 \pm 1.5	1.16 \pm 0.23	8/10	7/11 & 9/9	10662
60	49.5 \pm 3.1	1.14 \pm 0.28	9/9	8/10	10575
70	56.9 \pm 3.1	1.15 \pm 0.26	11/7	10/8 & 12/6	10466
80	62.5 \pm 1.9	1.17 \pm 0.17	12/6	11/7	10400
90	66.5 \pm 1.0	1.14 \pm 0.27	13/5	12/6	10327
100	71.4 \pm 1.6	1.18 \pm 0.22	18/0	-	9956

A plot of the average content of P12 in the GNCs against the feeding ratio (**Figure 1E**) revealed that the product line was mostly below the feeding line. Therefore, the C5 ligand appeared to bind more strongly to the gold kernel than P12, possibly because of the lower electrostatic repulsion among the C5 (neutral overall) over P12 (positively charged) ligands. The only exception was observed at a feeding ratio of 40%–45%, where the product composition (mainly $\text{Au}_{25}(\text{P12})_8(\text{C5})_{10}$) matched the feeding ratio, suggesting that the products of this ligand ratio were exceptionally stable.

Antibacterial screening

The antibacterial activity of GNCs was assessed using a few common Gram-positive (*Staphylococcus aureus* and MRSA) and Gram-negative (*Escherichia coli*, *Klebsiella pneumonia* and *Pseudomonas aeruginosa*) species (**Table 2** [16 h] and **SI, Table S2** [24 h]). The relationship between the antibacterial activity and the P12 ligand feeding ratio (*i.e.* surface positive charge density) of GNCs was interesting: first, the activity increased with the increasing P12 ligand feeding ratio (up to 50%), then there was a slight decrease (from 50% to 70%), and finally it increased again (from 70% to 100%). This trend was totally unexpected; since the antibacterial properties of GNC was mainly derived from the incorporated, positively charged P12 ligands, and not the C5 ligands; we had anticipated the



antibacterial activity to be positively correlated with the P12 content (GNC surface positive charge density). The fact that the GNC with a 50% P12-feeding ratio exhibited comparable antibacterial activity to that with 100% P12 ligand suggests that there must be an optimal window to tune the GNC antibacterial properties and biocompatibility.

Table 2. Antibacterial activity of different GNCs against five common pathogens (the colour code represents the antibacterial activity: red for high, yellow for medium, green for low and grey for negligible, and the same below).

P12 ratio in feeding (%)	*MIC ($\mu\text{g mL}^{-1}$ of GNC)				
	** <i>E. coli</i>	<i>K. pneumoniae</i>	<i>P. aeruginosa</i>	*** <i>S. aureus</i>	MRSA
0	>128	>128	>128	>128	>128
10	>128	>128	64	64	128
20	128	128	64	64	64
30	>128	>128	32	64	64
40	128	128	64	32	32
45	32	64	32	8	16
50	32	32	16	8	8
60	64	64	16	32	32
70	64	64	32	16	16
80	64	64	32	16	32
90	32	32	8	16	32
100	32	32	32	8	8

*MIC—Minimum inhibitory concentration

***Escherichia coli*, *Klebsiella pneumoniae*, *Pseudomonas aeruginosa* are Gram-negative bacteria.

****Staphylococcus aureus* and Methicillin-resistant *Staphylococcus aureus* (MRSA) are Gram-positive bacteria.

Table 2 reveals that the GNCs were more potent towards Gram-positive strains than towards Gram-negative ones. This phenomenon can be attributed to the differences in the surface structure between Gram-positive and -negative bacteria. The surface of Gram-positive bacteria is negatively charged,³⁸ thus, they exhibit a strong electrostatic interaction with cationic materials. For example, wall teichoic acid (WTA), a distinct cell wall component in Gram-positive bacteria, consists of repeating poly(glycerol phosphate) units and a phosphodiester terminus. WTA constitutes the polyanionic network, making the cell envelope highly negatively charged and susceptible to the binding of cationic materials.^{39,40} Besides, anionic lipids, such as phosphatidylglycerol (PG) and cardiolipin, constitute ~80% of the total lipids in Gram-positive bacterial membranes but only ~30% in Gram-negative strains.^{41,42} Moreover, negatively charged phospholipids, such as PGs, are present on both sides of bacterial cell membranes rather than only the inside membrane found on mammalian cells. This difference can provide selectivity between mammalian cells and bacteria for some positively charged antibacterial agents.⁴³

Table 3. The antibacterial activity toward Gram-positive bacteria of selected GNCs.

P12 ratio in feeding (%)	MIC ($\mu\text{g mL}^{-1}$ of GNC)							
	<i>S. aureus</i>	MRS A	<i>S. epidermidis</i>	MRS E	<i>S. haemolyticus</i>	MDR <i>S. haemolyticus</i>	<i>E. faecium</i>	VRE
45	8	16	8	8	32	32	32	16
50	8	8	8	8	32	32	32	16
100	8	8	4	4	8	8	16	16

As shown in **Table 2**, the three best-performing GNCs (45%, 50% and 100% P12 feeding ratio) were selected for further tests using more Gram-positive strains, including *Staphylococcus epidermidis*, *Staphylococcus haemolyticus*, *Enterococcus faecium* and their corresponding drug-resistant strains (MRSE, MDR *S. haemolyticus* and VRE). **Table 3** reveals that although the GNCs with 100% P12 exhibited the best antibacterial potency among the three groups, especially against MRSE, those with 45% and 50% P12 feeding also showed similar activity. These results further affirmed that antibacterial potency is not linearly correlated to the active P12 ligand content. Besides, during antibacterial tests, we observed aggregation of GNCs only with $\geq 60\%$ P12 in feeding in LB culture media, suggesting significant non-specific interactions with negatively charged serum proteins in cell culture media, which could adversely affect their antibacterial potency. This result was consistent with their high positive zeta potentials. This represents a key drawback for such strongly positively-charged GNCs and other nanomaterials, which can greatly limit their applications as antibacterial reagents (**SI**, **Figure S12**). Therefore, in synthesising mixed ligand-capped GNCs, we must balance the active/inert ligand (P12/C5 here) ratio and determine their actual antibacterial properties in order to find out the optimal ligand ratio.

Biocompatibility and cytotoxicity

To determine the optimal ligand ratio, we performed a haemolytic test (**SI**, **Figure S13**). The resulting HD_5 (the GNC dose that causes 5% haemolysis value against the P12 ligand-feeding ratio) was calculated for optimising the P12 feeding ratio (**Figure 1F**). The GNC haemolytic efficiency was enhanced (HD_5 reduced) with the increasing P12 ligand content, which also indicated that increasing the ZW ligand ratio could reduce the cytotoxicity of GNCs. The GNC prepared with 45% P12 still maintained a relatively high HD_5 of $34 \mu\text{g mL}^{-1}$, about twice that of the GNC prepared with 50% P12, while retaining almost the same MIC. Accordingly, GNCs prepared with $>45\%$ P12 could be too cytotoxic, thus unfavourable for *in vivo* applications. To determine the optimal P12 feeding ratio, we plotted the HD_5/MIC ratio versus P12 feeding ratio to collectively depict the change of biosafety and antibacterial activity of dual ligand GNCs. When the feeding ratio of P12



approached 45%, a sharp peak appeared, indicating GNC prepared with 45% P12 in feeding has a high antibacterial ability (low MIC) while maintaining low haemolytic activity (high HD₅), hence high biosafety, which is important for biomedical applications. This result also highlighted the importance of incorporating a certain proportion of ZW ligand in order to maintain good overall biocompatibility.

We further evaluated the cytotoxicity of GNCs prepared with 45% and 50% P12 ligand toward human umbilical vein endothelial cells (HUVECs). Compared with the 50%-P12 GNC, HUVECs demonstrated a much higher tolerance toward the 45%-P12 GNC (Figure 1G), indicating a striking shift in cytotoxicity as the P12 feeding ratio reaches 50%. This result is consistent with the significantly lower HD₅ value for the 50% P12 GNC observed above.

The use of excess cationic P12 ligand on GNC capping can lead to high cytotoxicity, adversely affecting its potential for *in vivo* application. However, too low the P12 ligand content can lead to low antibacterial activity. The key here is to balance the active/inert ligand ratio to achieve high stability and biocompatibility without compromising antibacterial potency. The above results comprehensively proved that GNCs prepared with 45% P12 feeding ligand displayed excellent antibacterial activity, low cytotoxicity, and good stability. Therefore, the 45% P12 ligand-feeding ratio was considered optimal for preparing GNCs (denoted as GNC hereafter) for subsequent analyses.

Combinational antibacterial analyses

We considered that, besides the direct killing of bacteria, GNC could sensitise drug-resistant bacteria toward varied antibiotics to restore their antibacterial potency.⁴⁴ To investigate this potential, we selected MRSE as the model microbe, to which our GNC demonstrated high inhibition. Seven antibiotics used to treat Gram-positive bacterial infections from four main categories: β -lactams (penicillin and carbapenem), glycopeptide, macrolides and tetracycline were tested. The result demonstrated that, except for vancomycin and tetracycline, all the other antibiotics exhibited low efficacy against this bacterial strain, with minimum inhibition concentrations (MICs) value $\geq 32 \mu\text{g mL}^{-1}$ (SI, Table S3). The test revealed high drug resistance of MRSE to several antibiotics.

A checkerboard method was further employed to evaluate the antibacterial properties of GNC and antibiotic combinational therapy.^{45,46} Imipenem (Imp), oxacillin (Oxa) and erythromycin (Ery), representing three classes of antibiotics, were applied with and without the GNC. Then, the fractional inhibitory concentration index (FICI) was calculated after 24 h of incubation. The calculated FICIs show that in joint applications, GNC exhibited the additive antibacterial ability with all three antibiotics (Figure 2A). Particularly, the Oxa group showed an exciting 128-fold decrease in antibiotic dosage needed to inhibit bacterial growth compared to the application of the antibiotic alone.

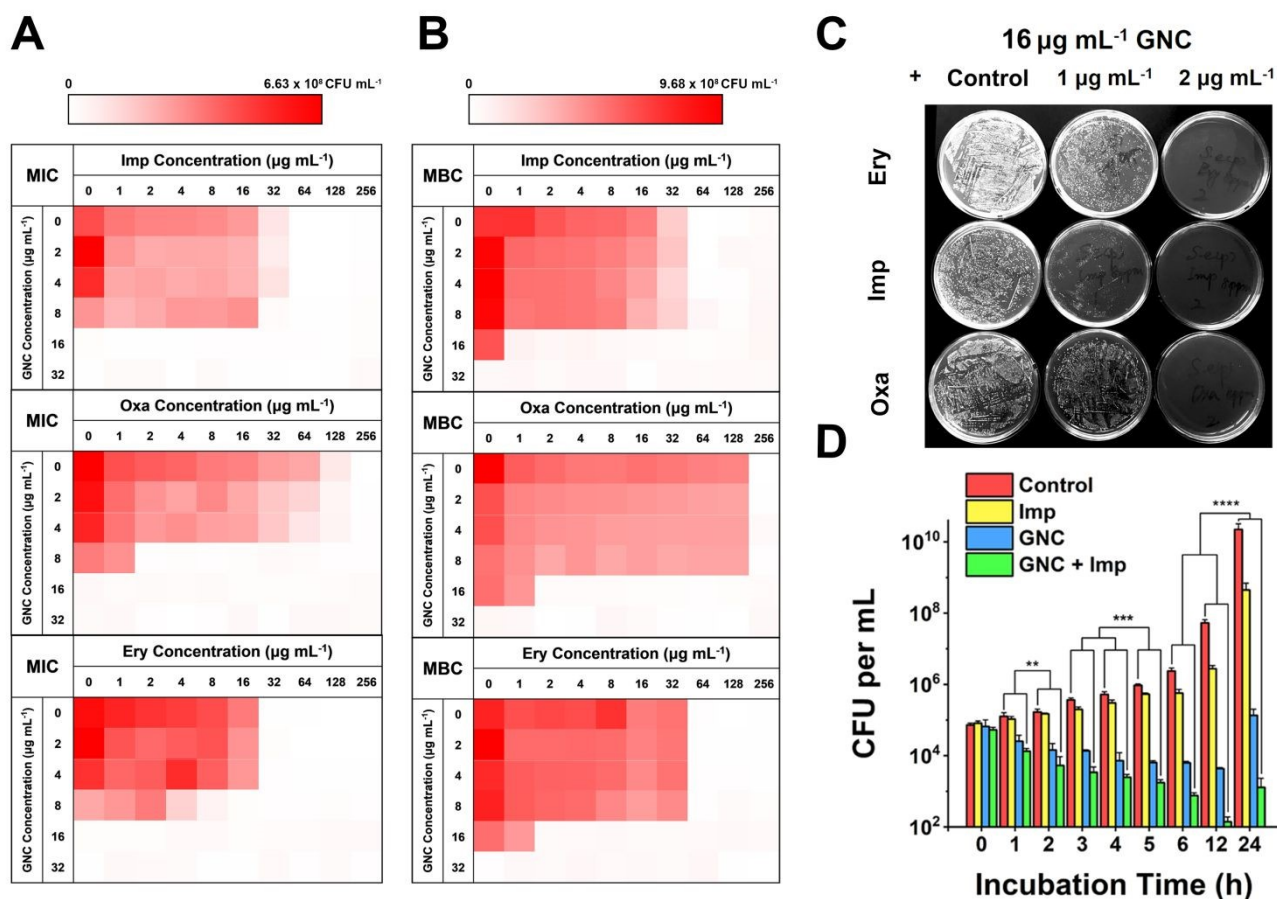


Figure 2. Combinational antibacterial assay of GNC with antibiotics. (A) 24-h checkerboard results of the GNC with imipenem (Imp), oxacillin (Oxa), and erythromycin (Ery) (OD_{600} values are given in the colour scale, a darker colour represents a higher bacteria concentration). The FICI was 1, 0.508, and 0.75 for GNC and Imp, Oxa, and Ery, respectively. (B) 48-h checkerboard results of GNC with Imp, Oxa, and Ery. The FICI was ~ 0.5 for all three groups. This experiment revealed the combination bactericidal effect of GNC with varied types of antibiotics. (C) Undiluted plate-coating results of MRSE colonies after treatment with PBS buffer (control), different concentrations of Ery/Imp/Oxa and $16 \mu\text{g mL}^{-1}$ GNC to visually display changes in colonies. (D) Time-killing curves demonstrate a superior antibacterial efficiency of the combination of GNC and Imp compared to their separate applications. PBS buffer (control), Imp only ($2 \mu\text{g mL}^{-1}$), GNC only ($16 \mu\text{g mL}^{-1}$), and a combination of GNC ($16 \mu\text{g mL}^{-1}$) and Imp ($2 \mu\text{g mL}^{-1}$) ($n=3$, ** $0.01 < P < 0.05$, *** $P < 0.01$ and **** $P < 0.001$).

We further prolonged the incubation to 48 h and re-measured FICI for each group (Figure 2B). The FICIs of all three groups were closer to 0.5, indicating the additive effect of GNC and antibiotics was enhanced. Specifically, adding $16 \mu\text{g mL}^{-1}$ of GNC and $2 \mu\text{g mL}^{-1}$ of any of the three tested antibiotics could prevent the growth of MRSE. We further took out the bacterial mixture and spread it onto agar plates to check the survival of MRSE and the agar plates remained unstained for the test groups compared with innumerable colonies for PBS control (Figure 2C). The results indicated that GNC had a remarkable ability to re-sensitise MRSE toward several antibiotics. Owing to the higher bactericidal efficiency, Imp was selected as the model antibiotics for further studies.

The MRSE-killing efficiency of this combination was measured by plotting the time-dependent killing graph (Figure 2D and SI, Figure S14). Compared to the PBS control, adding Imp did not significantly inhibit bacterial growth due to inherent high drug resistance. However, the GNC alone showed considerable bactericidal properties, giving rise to 10^5 -fold lower MRSE densities at 24 h. The combined group showed the best results, where the amount of MRSE colony was ~ 40 and 100 -fold lower than that of the GNC-only group at 12 and 24 h, respectively. Impressively, the bacterial count of the GNC+Imp combination group was more than 10^7 -fold lower than that of the control group at 24 h, demonstrating an excellent additive potency of the combined GNC and Imp in MRSE killing.

Antibacterial mechanisms

In general, cationic membrane-active molecules can exert several mechanisms to affect bacterial membrane function, for instance, attracting phospholipids to form defects and membrane leakage or perturbing membranes to induce lipid flip-flop.⁴² The damaged membrane causes detrimental membrane de-polarisation and spillage of cell contents, allowing antibiotics to penetrate the impaired bacterial

defence for swift killing.⁴⁷ The SEM images of MRSE cells revealed significant morphological differences after each different treatment (Figure 3A). For the negative control, all MRSE cells were spherical without apparent broken parts or wrinkles. Almost identical morphologies were observed for the Imp group, suggesting that the treatment with Imp alone did not cause noticeable damage to MRSE cells. In contrast, the GNC-treated group showed significantly altered cell morphologies and collapsed structures. The treated MRSE cells were tightly clustered together on a larger scale. A closer view revealed that the surface was covered with small grooves and wrinkles, indicating viability loss. This phenomenon was even more evident for the combined group (indicated with red arrows), where the grooves and wrinkles were deeper with a concave surface, indicating that the GNC+Imp combination could effectively agglutinate and deform bacterial cells, resulting in efficient bacterial killing.

After treatment with GNC+Imp, the MRSE cells formed irregular clusters which could hinder migration. This phenomenon was further confirmed by the corresponding NIR fluorescence image of the aggregated MRSE cells (Figure 3B). This result indicated that GNCs covered the envelope of MRSE cells, allowing them to aggregate by neutralising their surface negative charges and form 'bacterial clusters' to limit spread and prolong the interaction.

TEM images (Figure 3C) further confirmed the interaction of GNC with MRSE cells, which demonstrated the adhesion and penetration of GNCs within the cell envelope. Compared with the intact shape and apparent division septa for bacterial cells in the control group, the GNC+Imp treated group showed an abnormal cell division phenomenon: uneven division and empty cell walls were observed. Moreover, GNCs were mainly distributed within particular spaces on the cell envelope, indicating specific binding (indicated with red arrows).⁴⁸

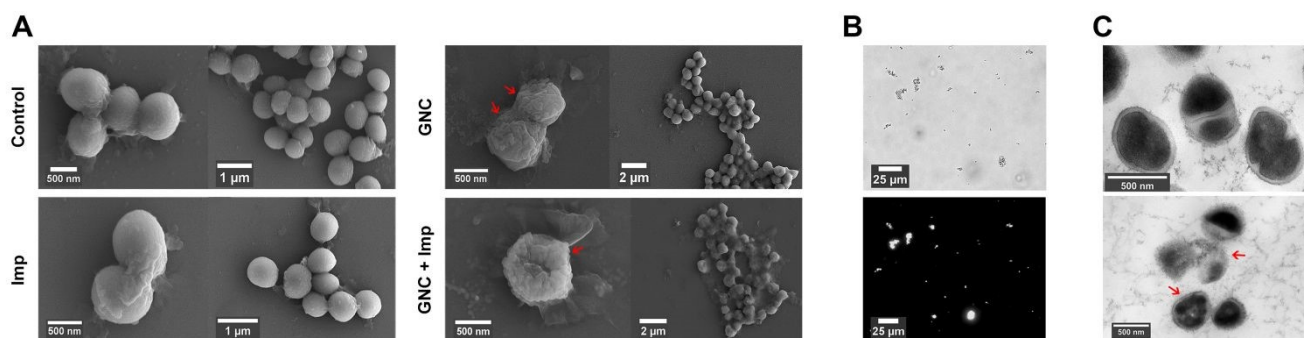


Figure 3. GNC antibacterial mechanism investigation. (A) Typical SEM images of MRSE after a 4-h treatment of PBS buffer (control), $2 \mu\text{g mL}^{-1}$ Imp, $16 \mu\text{g mL}^{-1}$ GNC, and a combination of Imp ($2 \mu\text{g mL}^{-1}$) and GNC ($16 \mu\text{g mL}^{-1}$). (B) Bright-field image (upper) and the corresponding NIR fluorescence image (lower) show that the GNC+Imp treated MRSE bacteria were extensively aggregated. (C) TEM images of PBS buffer (control group, upper) and $16 \mu\text{g mL}^{-1}$ GNC + $2 \mu\text{g mL}^{-1}$ Imp-treated MRSE (lower).



The antibacterial mechanism of GNC was further investigated. Although GNC binding-induced bacterial aggregation was already observed, it is still useful to investigate the specific binding target. The high abundance of negatively charged WTA may serve as a binding target for the positively charged GNCs via electrostatic interactions. Isothermal titration calorimetry (ITC) was conducted between GNCs and WTA, which revealed a multiple-binding endothermic interaction (SI, Figure S15A), indicating that WTA could initiate bacteria–GNC interactions.⁴⁹ To further verify this, a fluorescence competition assay with TR-Cadaverine was carried out. This dye can form a complex with WTA to quench its fluorescence. If GNC can compete with TR-Cadaverine in binding with WTA, adding GNC would result in dye release and fluorescence recovery. Figure S15B (SI) shows that the fluorescence of TR-Cadaverine significantly increased with an increase in GNC concentration and was saturated at $\sim 8 \mu\text{g mL}^{-1}$. Further increasing the GNC concentration could quench the dye fluorescence, possibly via dynamic quenching at high concentrations.⁵⁰ These results confirmed that WTA was a binding target for the GNC.

The 45% P12-feeding ratio yielded $\text{Au}_{25}(\text{P}12)_8(\text{C}5)_{10}$ as the primary product. Thus, we used this structure to simulate GNC binding with WTA by molecular binding simulation.⁵¹ A surface coverage state was established by simulating the GNC configurations (Figure 4A). Due to the electrostatic attractions between the cationic pyridinium and terminal anionic sulfonate groups, the ligands on the GNC surface are bended rather than pointing outward and form a ‘cage-like’ cap to stabilise the entire structure. This configuration explains the relatively high stability of GNC. Upon mixing with WTA, the electrostatic interactions between the GNC surface pyridinium groups and WTA phosphonate groups appeared to support GNC invasion of the bacterial cell envelope (Figure 4B). During this process, the cationic ligands interacted with the oppositely charged WTA layer, whereas the C5 ligands mainly pointed away from the surface. The initial electrostatic interactions further promote extensive contacts among the non-charged areas and strengthen their interactions via Van der Waals forces, which eventually contribute $\sim 57\%$ of the overall interaction (Figure 4C). Moreover, the weak hydrogen bonding between the WTA hydroxyl groups and pyridinium π -ring can further enhance the interaction (Figure 4D). WTA plays a vital role in drug resistance by providing attaching sites for other proteins that can replace synthases inhibited by penicillin antibiotics.⁴⁵ Thus, the binding of GNCs to WTA may compromise the bacterial drug resistance and partially explain the sensitisation of MDR stains towards antibiotics when co-treated with GNCs.

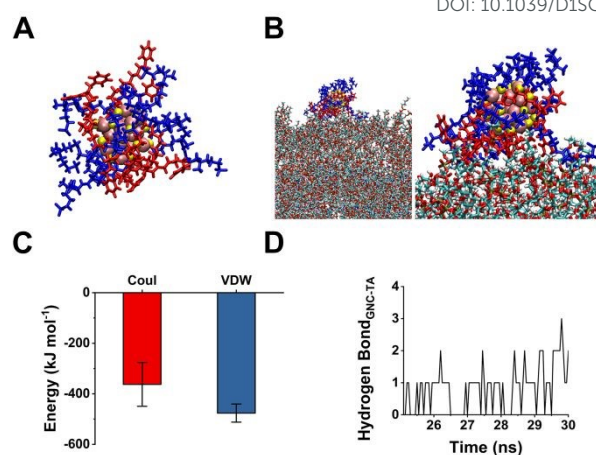


Figure 4. (A) Snapshot structure of an $\text{Au}_{25}(\text{P}12)_8(\text{C}5)_{10}$ cluster obtained: Blue indicates C5; red indicates P12; yellow indicates thiol groups; pink indicates gold atoms. (B) Left: Snapshot of the GNC interaction with the WTA; right: scaled-up illustration of the interacting part. (C) Interaction energy between GNC and WTA. Coul represents Coulomb force, while VDW denotes Van der Waals force. (D) Number of hydrogen bond interactions between GNC and WTA units over 5-ns simulation.

Upon binding to the bacterial cell membrane, the positive charges on the GNC could induce membrane potential dissipation and cause cell death. In this study, the membrane potential was determined by measuring the ratio of green to red fluorescence using a fluorescent kit to stain the bacteria, where the green to red fluorescence ratio is linear with the membrane potential dissipation rate (Figure 5A and B). Adding only Imp did not cause a significant upheaval of green fluorescence, indicating that Imp had no apparent effect on the bacterial membrane potential. However, a sharp decrease in the red fluorescence and an increase in green fluorescence were observed for the GNC-treated MRSE cells, suggesting significant membrane potential dissipation. Membrane potential dissipation can severely interfere with normal physiological activities and cause cell death; thus, this result was consistent with the SEM and TEM images. Moreover, clustered bacteria were also observed in the GNC groups, indicating that membrane potential dissipation was related to the GNC-induced bacterial agglomeration.⁵²

Inserting positively charged amphiphilic material has been shown to lysis cell membranes.^{53,54} The collapse of the MRSE cell structure, as observed in the SEM images, indicated that GNC could affect cell envelope completeness. To investigate whether the GNC treatment affected the integrity of cell membranes, we used a cell-integrity analysis kit, in which the dye can penetrate damaged membranes and bind to intracellular proteins. A positive correlation between the GNC concentration and dye incorporation confirmed that GNC could damage the integrity of the cell membrane (Figure 5C). The GNC+Imp combination exhibited even higher membrane permeation than the GNC-only treatment, consistent with the superior bactericidal potency. The antibacterial mechanism of Imp is to inhibit the synthesis of cell walls, thereby bursting the bacterial cells. By damaging bacterial cell membrane, GNC can



effectively enhance antibiotics transverse bacterial cell membranes, resulting in the additive bactericidal potency. GNCs have been shown to generate ROS, which has bactericidal effects.¹² Therefore, we studied ROS generation in all treatments (Figure 5D). Imp alone did not produce significant ROS, whereas GNC exhibited a good ability to generate ROS. Further addition of Imp did not increase ROS production. Therefore, only GNC is responsible for ROS production in the GNC+Imp combination. To investigate the exact species of ROS responsible here, we used two test kits to detect common ROS species, $\bullet\text{O}_2^-$ and $\bullet\text{OH}$ (Figure 5E). There was an increase in the production of $\bullet\text{O}_2^-$ but not $\bullet\text{OH}$ in the GNC treatments (Figure 5F). Hence, $\bullet\text{O}_2^-$ was confirmed to be the ROS species generated by the GNC treatment. Its high reactivity can damage cell membranes and other essential biological macromolecules to exert bactericidal effects. Some ROS-generating antibacterial materials have been found to have higher antibacterial activities on Gram-positive over Gram-negative strains, allowing them to be even used as Gram-selective staining reagents^{55,56,57}. The ROS generation ability of our GNC may also account for its higher antibacterial effect towards Gram-positive species like MRSE or *S. aureus* over Gram-negative ones.

Based on the above experimental results, our GNC exhibits four antibacterial mechanisms. 1) by binding to WTA, the GNC could interact and aggregate bacterial cells to control their spread and initiate subsequent antibacterial steps. 2) Its positive charges can interrupt the bacterial membrane potential, which may interfere with bacterial normal functions by disrupting the functions of some crucial enzymes⁵⁸. 3) Simultaneously, the amphiphilic cationic ligands can disrupt the cell membrane, thus enhancing the permeation of antibiotics and improving their bactericidal effect, which, we believe, is the most important antibacterial mechanism of our GNCs⁵⁹. 4) It can effectively generate ROS to damage the bacterial membrane and other vital genetic and cellular molecules. Combining all four bactericidal actions, the combination of GNC and antibiotics can effectively eliminate Gram-positive MDR bacteria like MRSE.

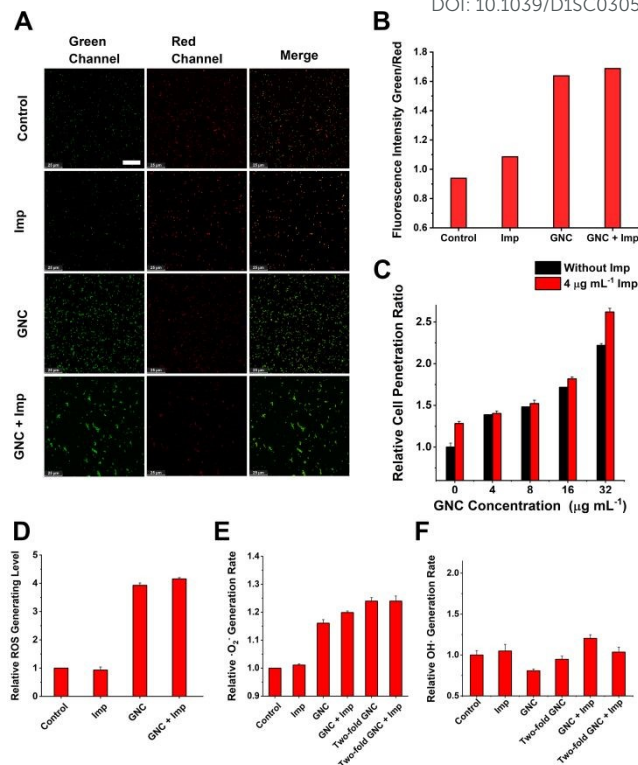


Figure 5. Investigating other possible antibacterial properties. (A) Membrane potential of MRSE cells after treatment in PBS buffer (control), $4 \mu\text{g mL}^{-1}$ Imp, $16 \mu\text{g mL}^{-1}$ GNC, and a combination of Imp ($4 \mu\text{g mL}^{-1}$) and GNC ($16 \mu\text{g mL}^{-1}$) (scale bar: $25 \mu\text{m}$). (B) Comparison of the green-to-red fluorescent intensity ratios in different groups. (C) Comparison of the cell penetration rate at different concentrations of GNC with/without the addition of $4 \mu\text{g mL}^{-1}$ Imp ($n=4$). (D) Total ROS generation rate for the combination group compared with PBS control and individual application ($n=3$). (E) Superoxide anion generation rate of the combination group, the PBS (control) and single applications ($n=3$). (F) ROS colourimetric analysis results with the nitro-blue tetrazolium (NBT) method, which demonstrates no correlation between $\bullet\text{OH}$ generation rate and the addition of GNC and Imp ($n=3$).

Stability and cytotoxicity evaluation

The cytotoxicity of combined therapy on somatic (NIH 3T3 and HUVEC) cell lines was investigated by Calcein-AM/propidium iodide staining, where live/dead cells were stained in green/red, respectively. Confocal fluorescence images (SI, Figure S16A and B) reveal that most cells were alive with hardly noticeable numbers of dead cells, suggesting that both cell lines maintained high viability after 24-h incubation with $70 \mu\text{g mL}^{-1}$ of GNC + $30 \mu\text{g mL}^{-1}$ Imp. This was further verified by live-cell counting (SI, Figure S16C), where the percentage of live cells were above 80%, comparable to that of the controls.

The stability of nanomaterials in storage is a crucial for its potential practical applications. We measured the UV-vis spectrum of freshly prepared GNC solution and after 3-month storage at $4 \text{ }^\circ\text{C}$ in a normal refrigerator (SI, Figure S17). We did not observe any deformation nor emergence of new peaks in the UV-vis spectrum. In addition, there were no changes in the physical appearance, aggregation, or precipitation, confirming the good stability of the GNC.

NIR-II fluorescence is an attractive imaging modality that is well suited for *in vivo* applications. Owing to its attractive NIR fluorescence, GNC can act as fluorescent probes for organ



View Article Online
DOI: 10.1039/D1SC03056F

distribution tracking.⁶⁰ We evaluated the GNC stability *in vitro* using simulated biological fluids. The GNC fluorescence ($128 \mu\text{g mL}^{-1}$) was highly stable and showed no observable changes after 15-day incubation in PBS supplemented with up to 10% human serum albumin (HSA, see **SI, Figure S18**). Thus, its stable NIR fluorescence can be used to directly evaluate the GNC organ distribution with a NIR animal imager using 808-nm laser irradiation (**Figure 6A**). Upon intravenous injection of GNC+Imp, strong NIR fluorescence was observed primarily in the liver with weak signals in the spleen and kidneys within the first hour, suggesting preferential accumulation in these organs. The NIR fluorescence in the main organs was maintained for 10 h, then it gradually faded away after 24 h

and became almost invisible at 96-h post-injection, indicating that most of the GNCs were cleared from the body. The gold contents measured from critical organs harvested at different post-injection times were consistent with the NIR fluorescence results (>80% of the Au contents were cleared after 96 h, **Figure 6B**). These results indicate that the GNC has an adequate body clearance time and is suitable for intravenous administration. Moreover, the blood routine as well as liver and kidney function indicators further confirmed that a high dosage of GNC+Imp did not induce any notable change when compared with the control group, suggesting minimal *in vivo* toxicity (**SI, Figures S19 A–F**).



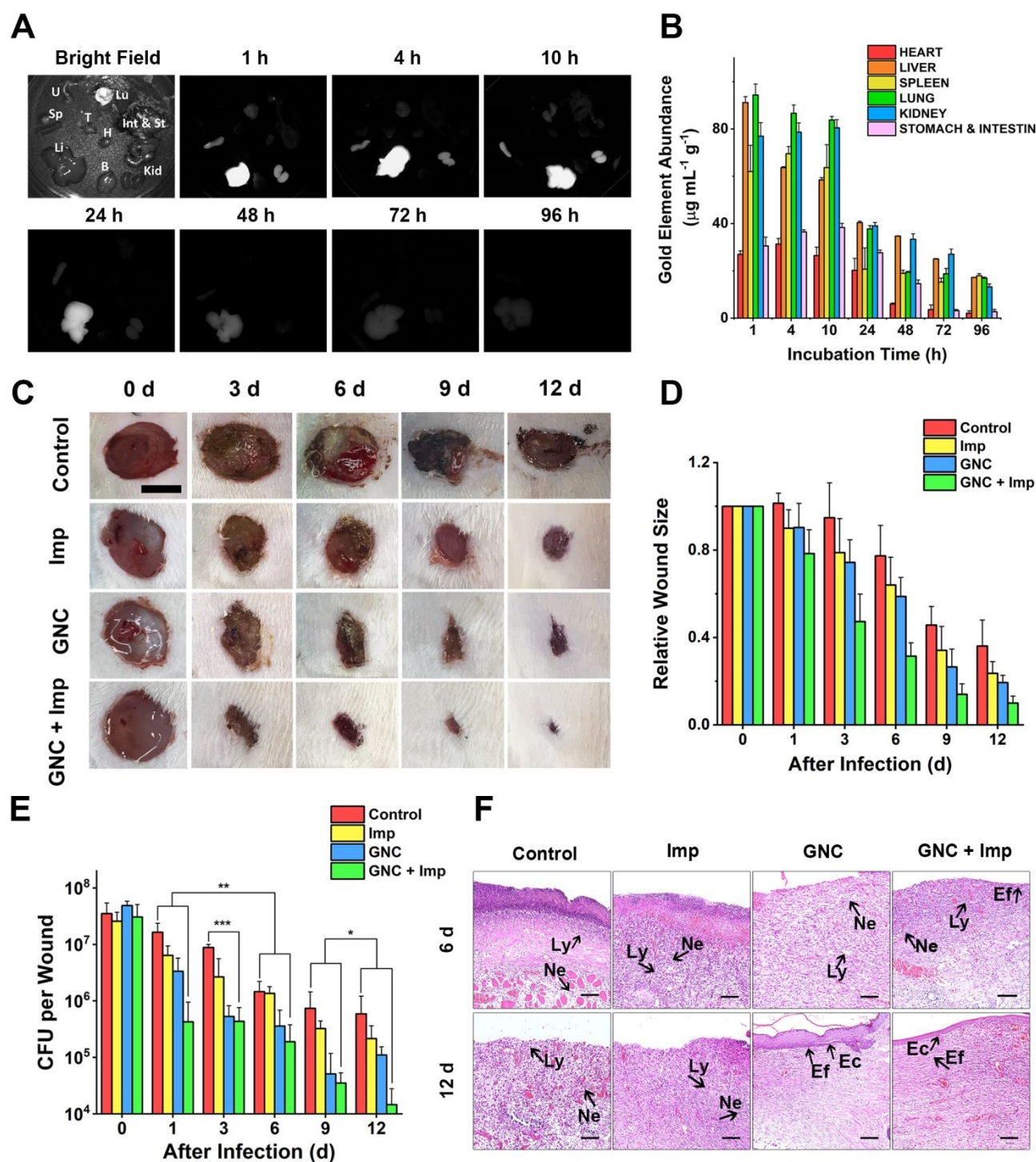


Figure 6. *In vivo* experiments demonstrate the appropriate clearance time and effective treatment effect. (A) NIR fluorescence of crucial organs of mice harvested at different time points under bright-field and 808-nm laser radiation (B: Brain, H: Heart, Int & St: Intestine and Stomach, Kid: Kidneys, Li: Liver, Lu: Lungs, Sp: Spleen, T: Thymus and U: Uterus). (B) Gold content (average weight) in different organs, harvested at different times post-injection ($n=4$). (C) Representative images of changes in wound size in different groups within 12 days post-treatment (scale bar: 10 mm). (D) Comparison of the relative wound size vs. time in different groups: PBS (control), $24 \mu\text{g mL}^{-1}$ Imp solution, $64 \mu\text{g mL}^{-1}$ GNC solution, and the combination of $24 \mu\text{g mL}^{-1}$ Imp ($\sim 0.12 \text{ mg kg}^{-1}$, final concentration) and $64 \mu\text{g mL}^{-1}$ GNC solution ($\sim 0.32 \text{ mg kg}^{-1}$, final concentration, same below) ($n=3$); (E) Plate coating results of the PBS control, single application, and combined therapy groups ($n=3$, $*P > 0.05$, $** 0.01 < P < 0.05$ and $***P < 0.01$). (F) The hematoxylin-eosin staining graphs in different groups. After 12 days, the epidermis was fully reconstructed in the GNC+Imp group (Ly: lymphocytes; Ne: neutrophil; Ec: epithelial cell and Ef: elongated fiber).



Skin infection model experiments

As a coagulase-negative strain, MRSE can cause soft tissue and skin infections and frequently induces infection in surgical site⁵; thus, we established a skin infection model by creating wounds with removal of epidermis and dermis on the back of rats and infecting them with MRSE, to which conventional wound treatment methods are difficult to sustain antibacterial ability. Different groups were treated with either PBS control, Imp only, GNC only or GNC+Imp. The effect was monitored by measuring the wound size and bacterial counts after plate coating. Compared with the negative control, the wound healing rate for the rats treated with either Imp or GNC was higher. Notably, the wound healing of the GNC+Imp combinational group was the fastest. The size of the wound was significantly smaller than that of other groups, and the normal skin was almost fully reconstructed in 9 days (Figure 6C and D). Moreover, the scab size was significantly smaller than other groups, indicating a markedly reduced bacterial infection.

To quantify the clearance of bacteria on the skin wound, we performed plate coating to compare the number of colonies on differently treated wounds (Figure 6E). The MRSE counts of the negative control and Imp groups were slowly reduced over time due to autoimmunity, and the GNC-treated group showed a more significant decrease. Treatment with GNC+Imp resulted in the most rapid reduction of the bacterial population, and by day 12, the bacterial count was >10-fold lower than that of the GNC-only group and almost two orders of magnitude lower than that of the negative control group. This *in vivo* result was consistent with the superior *in vitro* antibacterial potency of GNC+Imp over that of GNC or Imp only. Pathological analyses further confirmed a complete repair of the wound tissue for the GNC+Imp group but not for the negative control and GNC- or Imp-only groups. The reconstruction of well-stratified skin layers and significantly reduced immune cells indicated the successful removal of the lesions in the GNC+Imp group (Figure 6F).

Conclusion

In this study, we synthesised a series of formula-defined pyridinium-zwitterionic ligand-functionalised Au₂₅(SR₁)_x(SR₂)_{18-x} GNCs as antibacterial nanomaterials. By fine-tuning the feeding ligand ratios, we obtained GNCs that exhibited both excellent antibacterial ability and high stability, successfully addressed a major issue in antibacterial gold nanomaterials development. Besides, the GNCs exert multiple antibacterial mechanisms, giving rise to high potency against Gram-positive MDR bacteria. The optimized GNC can significantly reduce the dosage of antibiotics required to treat MDR bacterial infections, thereby greatly enhancing the efficacy of frontline antibiotics. Compared to other nanomaterials without defined chemical formulas, which could cause difficulties in quality control and mechanism research, our Au₂₅(SR₁)_x(SR₂)_{18-x} GNCs are potentially better suited for medical applications. Moreover, biocompatible Au₂₅ GNCs capped with two, or more ligands can incorporate more

functions, thus widening the scope of its biomedical applications. We envisage that dual/multi-ligand-functionalised GNCs would find broad applications in chemistry, physics, biology, and biomedical sciences.

Conflicts of Interest

The authors declare no competing financial interest.

Acknowledgements

We acknowledge the financial support from the Shenzhen Science and Technology Programme (KQTD20190929172743294). This work was partly funded by the UK Biotechnology and Biological Sciences Research Council (grant no: BB/R007829/1 to DZ).

Notes and References

- 1 P. Fernandes, *Nat. Biotechnol.*, 2006, **24**, 1497–1503.
- 2 W. Cassandra, *Nature*, 2017, **543**, 15.
- 3 L. Wang, C. Hu and L. Shao, *Int. J. Nanomedicine.*, 2017, **12**, 1227–1249.
- 4 M. Otto, *Nat. Rev. Microbiol.*, 2009, **7**, 555–567.
- 5 L. M. Weiner-Lastinger, S. Abner, J. R. Edwards, A. J. Kallen, M. Karlsson, S. S. Magill, D. Pollock, I. See, M. M. Soe, M. S. Walters and M. A. Dudeck, *Infect. Control Hosp. Epidemiol.*, 2020, **41**, 1–18.
- 6 A. M. Hanssen, G. Kjeldsen and J. U. Ericson Sollid, *Antimicrob. Agents Chemother.*, 2004, **48**, 285–296.
- 7 U.S. Department of Health and Human Services, *Centers Dis. Control Prev.*, 2019, 1–113.
- 8 Z. Jiang, A. Sahar, X. Li, S. M. Robinson, V. M. Rotello, K. Saha, M. A. Riley, D. F. Moyano and A. Gupta, *ACS Nano*, 2014, **8**, 10682–10686.
- 9 A. Gupta, S. Mumtaz, C. H. Li, I. Hussain and V. M. Rotello, *Chem. Soc. Rev.*, 2019, **48**, 415–427.
- 10 H. T. T. Duong, N. N. M. Adnan, N. Barraud, J. S. Basuki, S. K. Kutty, K. Jung, N. Kumar, T. P. Davis and C. Boyer, *J. Mater. Chem. B*, 2014, **2**, 5003–5011.
- 11 K. Ma, Y. Li, Z. Wang, Y. Chen, X. Zhang, C. Chen, H. Yu, J. Huang, Z. Yang, X. Wang and Z. Wang, *ACS Appl. Mater. Interfaces.*, 2019, **11**, 29630–29640.
- 12 K. Zheng, M. I. Setyawati, D. T. Leong and J. Xie, *ACS Nano*, 2017, **11**, 6904–6910.
- 13 R. R. Nasaruddin, T. Chen, N. Yan and J. Xie, *Coord. Chem. Rev.*, 2018, **368**, 60–79.
- 14 Y. Xie, Y. Liu, J. Yang, Y. Liu, F. Hu, K. Zhu and X. Jiang, *Angew. Chem. Int. Ed.*, 2018, **57**, 3958–3962.
- 15 Y. Xie, W. Zheng and X. Jiang, *ACS Appl. Mater. Interfaces.*, 2020, **12**, 9041–9049.
- 16 M. Yu, J. Xu and J. Zheng, *Angew. Chem. Int. Ed.*, 2019, **131**, 4156–4172.
- 17 R. Jin, *Nanoscale*, 2015, **7**, 1549–1565.
- 18 X. Kang, H. Chong and M. Zhu, *Nanoscale*, 2018, **10**, 10758–10834.
- 19 Z. Yu, H. Xiao, X. Zhang, Y. Yang, Y. Yu, H. Chen, X. Meng,



- W. Ma, M. Yu, Z. Li, C. Li and H. Liu, *ACS Nano*, 2020, **14**, 13536–13547.
- 20 D. Li, Q. Liu, Q. Qi, H. Shi, E. C. Hsu, W. Chen, W. Yuan, Y. Wu, S. Lin, Y. Zeng, Z. Xiao, L. Xu, Y. Zhang, T. Stoyanova, W. Jia and Z. Cheng, *Small*, 2020, **16**, 1–9.
- 21 M. Petkovic, K. R. Seddon, L. P. N. Rebelo and C. S. Pereira, *Chem. Soc. Rev.*, 2011, **40**, 1383–1403.
- 22 P. K. Sreenivasan, V. I. Haraszthy and J. J. Zambon, *Lett. Appl. Microbiol.*, 2013, **56**, 14–20.
- 23 S. Chen, L. Li, C. Zhao and J. Zheng, *Polymer (Guildf.)*, 2010, **51**, 5283–5293.
- 24 J. Shaoyi and C. Zhiqiang, *Adv. Mater.*, 2009, **22**, 920–932.
- 25 A. K. Murthy, R. J. Stover, W. G. Hardin, R. Schramm, G. D. Nie, S. Gourisankar, T. M. Truskett, K. V. Sokolov and K. P. Johnston, *J. Am. Chem. Soc.*, 2013, **135**, 7799–7802.
- 26 Y. Guo, C. Sakonsinsiri, I. Nehlmeier, M. A. Fascione, H. Zhang, W. Wang, S. Pöhlmann, W. B. Turnbull and D. Zhou, *Angew. Chem. Int. Ed.*, 2016, **128**, 4816–4820.
- 27 Z. Luo, V. Nachammai, B. Zhang, N. Yan, D. T. Leong, D. E. Jiang and J. Xie, *J. Am. Chem. Soc.*, 2014, **136**, 10577–10580.
- 28 R. Jin, H. Qian, Z. Wu, Y. Zhu, M. Zhu, A. Mohanty and N. Garg, *J. Phys. Chem. Lett.*, 2010, **1**, 2903–2910.
- 29 H. Liu, G. Hong, Z. Luo, J. Chen, J. Chang, M. Gong, H. He, J. Yang, X. Yuan, L. Li, X. Mu, J. Wang, W. Mi, J. Luo, J. Xie and X. D. Zhang, *Adv. Mater.*, 2019, **31**, 1–9.
- 30 G. Hong, A. L. Antaris and H. Dai, *Nat. Biomed. Eng.*, 2017, **1**, 1–22.
- 31 A. L. Antaris, H. Chen, S. Diao, Z. Ma, Z. Zhang, S. Zhu, J. Wang, A. X. Lozano, Q. Fan, L. Chew, M. Zhu, K. Cheng, X. Hong, H. Dai and Z. Cheng, *Nat. Commun.*, 2017, **8**, 1–11.
- 32 Y. Sun, M. Ding, X. Zeng, Y. Xiao, H. Wu, H. Zhou, B. Ding, C. Qu, W. Hou, A. G. A. Er-bu, Y. Zhang, Z. Cheng and X. Hong, *Chem. Sci.*, 2017, **8**, 3489–3493.
- 33 F. Aldeek, M. A. H. Muhammed, G. Palui, N. Zhan and H. Mattoussi, *ACS Nano*, 2013, **7**, 2509–2521.
- 34 M. Song, G. Zhou, N. Lu, J. Lee, E. Nakouzi, H. Wang and D. Li, *Science*, 2020, **367**, 40–45.
- 35 Y. Ishida, K. Narita, T. Yonezawa and R. L. Whetten, *J. Phys. Chem. Lett.*, 2016, **7**, 3718–3722.
- 36 X. Yuan, B. Zhang, Z. Luo, Q. Yao, D. T. Leong, N. Yan and J. Xie, *Angew. Chemie - Int. Ed.*, 2014, **53**, 4623–4627.
- 37 T. Chen, V. Fung, Q. Yao, Z. Luo, D. E. Jiang and J. Xie, *J. Am. Chem. Soc.*, 2018, **140**, 11370–11377.
- 38 N. Malanovic and K. Lohner, *Biochim. Biophys. Acta - Biomembr.*, 2016, **1858**, 936–946.
- 39 L. Pasquina-Lemonche, J. Burns, R. D. Turner, S. Kumar, R. Tank, N. Mullin, J. S. Wilson, B. Chakrabarti, P. A. Bullough, S. J. Foster and J. K. Hobbs, *Nature*, 2020, **582**, 294–297.
- 40 Z. V. Feng, I. L. Gunsolus, T. A. Qiu, K. R. Hurley, L. H. Nyberg, H. Frew, K. P. Johnson, A. M. Vartanian, L. M. Jacob, S. E. Lohse, M. D. Torelli, R. J. Hamers, C. J. Murphy and C. L. Haynes, *Chem. Sci.*, 2015, **6**, 5186–5196.
- 41 P. Kumar, J. N. Kizhakkedathu and S. K. Straus, *Biomolecules*, 2018, **8**, 4.
- 42 R. M. R. F. Epand, C. Walker, R. M. R. F. Epand and N. A. Magarvey, *Biochim. Biophys. Acta - Biomembr.*, 2016, **1858**, 980–987.
- M. Zasloff, *Nature*, 2002, **415**, 389–395.
- Y. Zhao, Z. Chen, Y. Chen, J. Xu, J. Li and X. Jiang, *J. Am. Chem. Soc.*, 2013, **135**, 12940–12943.
- M. A. Foxley, S. N. Wright, A. K. Lam, A. W. Friedline, S. J. Strange, M. T. Xiao, E. L. Moen and C. V. Rice, *ACS Med. Chem. Lett.*, 2017, **8**, 1083–1088.
- J. Campbell, A. Singh, J. Santa Maria, K. Younghoon, S. Brown, J. G. Swoboda, E. Mylonakis, B. J. Wilkinson and S. Walker, *ACS Chem. Biol.*, 2010, **6**, 106–116.
- N. Zhang and S. Ma, *Eur. J. Med. Chem.*, 2019, **184**, 111743.
- S. C. Hayden, G. Zhao, K. Saha, R. L. Phillips, X. Li, O. R. Miranda, V. M. Rotello, M. A. El-Sayed, I. Schmidt-Krey and U. H. F. Bunz, *J. Am. Chem. Soc.*, 2012, **134**, 6920–6923.
- B. Wang, L. Zhang, C. B. Sung and S. Granick, *Proc. Natl. Acad. Sci. U. S. A.*, 2008, **105**, 18171–18175.
- B. Dubertret, M. Calame and A. J. Libchaber, *Nat. Biotechnol.*, 2001, **19**, 365–370.
- E. R. Caudill, R. T. Hernandez, K. P. Johnson, J. T. O'Rourke, L. Zhu, C. L. Haynes, Z. V. Feng and J. A. Pedersen, *Chem. Sci.*, 2020, **11**, 4106–4118.
- Z. Huang, Y. Liu, L. Wang, A. Ali, Q. Yao, X. Jiang and Y. Gao, *Biomaterials*, 2020, **253**, 120124.
- J. N. Pendleton and B. F. Gilmore, *Int. J. Antimicrob. Agents*, 2015, **46**, 131–139.
- A. Chomposor, K. Saha, P. S. Ghosh, D. J. Macarthy, O. R. Miranda, Z.-J. Zhu, K. F. Arcaro and V. M. Rotello, *Small*, 2010, **6**, 2246–2249.
- M. Kang, C. Zhou, S. Wu, B. Yu, Z. Zhang, N. Song, M. M. S. Lee, W. Xu, F. J. Xu, D. Wang, L. Wang and B. Z. Tang, *J. Am. Chem. Soc.*, 2019, **141**, 16781–16789.
- J. Li, H. Zhou, J. Wang, D. Wang, R. Shen, X. Zhang, P. Jin and X. Liu, *Nanoscale*, 2016, **8**, 11907–11923.
- R. J. Barnes, R. Molina, J. Xu, P. J. Dobson and I. P. Thompson, *J. Nanoparticle Res.*, 2013, **15**, 1432.
- Y. Cui, Y. Zhao, Y. Tian, W. Zhang, X. Lü and X. Jiang, *Biomaterials*, 2012, **33**, 2327–2333.
- M. Godoy-Gallardo, U. Eckhard, L. M. Delgado, Y. J. D. de Roo Puente, M. Hoyos-Nogués, F. J. Gil and R. A. Perez, *Bioact. Mater.*, 2021, **6**, 4470–4490.
- Y. Kong, J. Chen, H. Fang, G. Heath, Y. Wo, W. Wang, Y. Li, Y. Guo, S. D. Evans, S. Chen and D. Zhou, *Chem. Mater.*, 2016, **28**, 3041–3050.



View Article Online
DOI: 10.1039/D1SC03056F

Open Access Article. Published on 25 October 2021. Downloaded on 10/27/2021 1:45:50 PM.
This article is licensed under a Creative Commons Attribution-NonCommercial 3.0 Unported Licence.



Chemical Science Accepted Manuscript